JOURNAL OF THERMOPHYSICS AND HEAT TRANSFER
Vol. 35, No. 3,

Thermal Analysis of Calcium–Magnesium–Alumino–Silicate Infiltration Dynamics in Thermal Barrier Coatings

Timothy W. Munuhe,* Liang Zhu,† and Ronghui Ma‡
University of Maryland, Baltimore, Maryland 21250

https://doi.org/10.2514/1.T6171

Molten calcium–magnesium–alumino–silicate (CMAS) infiltration into thermal barrier coatings (TBCs) of gas turbines causes loss of strain tolerance and delamination of the ceramic topcoat. To develop efficient mitigation strategies, it is crucial to understand CMAS infiltration dynamics into the porous topcoat. This study introduces an integrated model, incorporating liquid flow in unsaturated porous structures, heat transfer, and temperature-dependent viscosities, to study CMAS infiltration through TBCs grown by the electron beam physical vapor deposition (EB-PVD) method. The effects of different CMAS compositions, temperature gradients across the topcoat, and coating microstructures are investigated. Our simulation shows that CMAS infiltration exhibits significantly nonlinear dynamics with a fast infiltration rate at the early stage due to high temperature, high pressure gradients, and low viscosity. Neglecting heat transfer enhancement from CMAS by approximating the temperature distribution as linear underestimates the infiltration rate. Fine porous microstructures slow infiltration, and bilayer or multilayer structures, consisting of variable column and pore sizes, combine the advantages of an increased hydraulic resistance to infiltration and lower capillary pressures. Such heterogeneous structures can delay early-stage infiltration by manipulating the layer thickness and arrangement. It is anticipated that the quantitative information and advanced understanding obtained would benefit the development of CMAS-resistant EB-PVD TBC topcoats.

Nomenclature

A, B, C	=	constants for viscosity model
c	=	color function
C_p	=	specific heat capacity, $\mathrm{J/(kg \cdot K)}$
D	=	characteristic length of columns, μm
dt	=	time step, s
h_p	=	infiltration depth, μm
i	=	time index during navigation
K	=	hydraulic permeability, $\mathrm{m^2}$
k	=	thermal conductivity, $\mathrm{W/(m \cdot K)}$
L	=	topcoat thickness, μm
P	=	pressure, kPa
r	=	radius, μm
T	=	temperature, °C
V	=	velocity, $\mu\mathrm{m/s}$
z	=	position, μm
ε	=	porous medium porosity
θ	=	contact angle, deg
μ	=	viscosity, $\mathrm{Pa \cdot s}$
ρ	=	density, $\mathrm{kg/m^3}$
σ	=	surface tension, $\mathrm{Pa \cdot m}$
τ	=	tortuosity

Subscripts

c	=	capillary
e	=	equilibrium
eff	=	effective
f	=	liquid
i	=	inner dimension, length
j	=	time index
L	=	at the bottom surface, where z is equal to L
m	=	solid matrix
o	=	outer dimension, length
p	=	porous medium
top	=	at the top surface, where z is equal to 0

Superscripts

I. Introduction

THERMAL barrier coatings (TBCs) on hot sections of gas turbine components, mainly turbine blades, provide thermal protection to metallic components by insulating them from hot and corrosive gas streams. The application of TBCs allows turbine inlet temperatures to be elevated beyond the tolerance of the turbine superalloy material, and substantially improves turbine efficiency, performance, and service life [1–5]. A typical TBC coating has a multilayer structure consisting of a thermally resistant ceramic topcoat, a metallic bond coat for reducing thermal expansion mismatch and providing oxidation/corrosion resistance, and a superalloy substrate. At the interface of the ceramic topcoat and the bond coat, a thermally grown oxide layer also forms in a high-temperature environment. The ceramic topcoat, commonly YSZ (ZrO_2 stabilized with 7–8 wt % Y_2O_3) with a thickness in the range of 100–400 μm [6–10], has a porous structure that improves thermal insulation as well as tolerance to thermal strain and stress induced by exposure to thermal cycling. The YSZ topcoats are commonly deposited either by air plasma spray (APS) or electron beam physical vapor deposition (EB-PVD), with differing microstructures for each method [11,12]. The EB-PVD method, which is the focus of the current study, grows columns using electron-beam-vaporized coat materials [12]. The column structures of the YSZ coat provide a higher thermal strain tolerance than the APS TBCs [10,12,13].

High turbine inlet temperatures raise a critical durability issue for aeroengines operating in dusty environments [14–17]. Aeroengines intake siliceous particles whose composition most commonly includes oxides of calcium, magnesium, aluminum, and silicon (CMAS). These particles can melt at temperatures above 1150°C [18–23]. The molten CMAS can deposit on hot TBC surfaces of the gas turbine and infiltrate into the porous YSZ topcoats. It may also react directly with the TBC constituents and cause destabilization of the TBC, accelerated oxidation, and hot corrosion of the underlying metallic bond coat and superalloy substrate [24–28]. Upon cooling, the infiltrated CMAS stiffens the YSZ layer, and the loss in strain and stress tolerance causes delamination of the top layer. The CMAS-associated corrosion and thermomechanical damage ultimately accelerate the failure of TBCs

Received 21 August 2020; revision received 17 November 2020; accepted for publication 19 November 2020; published online Feb epubMonth 2021.

*Ph.D. Candidate, Department of Mechanical Engineering.
†Professor, Department of Mechanical Engineering.
‡Associate Professor, Department of Mechanical Engineering.

and underlying components. Quantitative information on the CMAS infiltration in YSZ topcoats of various microstructures and thermal conditions is crucial to the development of strategies to mitigate the damage by CMAS attack.

CMAS infiltration into the pores of YSZ topcoats is mainly driven by capillary forces [24,27,29]. The penetrating rate is governed by multiple factors, including the structural characteristics of the ceramic layer, the temperature distribution, as well as the properties of the CMAS such as melting point, viscosity, and surface tension. Several studies have focused on understanding the infiltration behavior of CMAS in TBC topcoats by heating CMAS powder on top of a piece of a stand-alone YSZ topcoat layer in ovens maintained above the melting temperatures [6,17,22,23,30–32]. Naraparaju et al. [6,22,30–32] studied CMAS infiltration through YSZ layers of various columnar structures under isothermal conditions over the span of minutes to hours. Zhao et al. [10] investigated the effect of increasing the pore volume fraction upon silicate melt infiltration in a YSZ layer at 1250°C. There have been comparatively fewer attempts to consider the effect of temperature gradients in the TBC on the CMAS infiltration process. Jackson et al. [33,34] examined the effect of temperature gradients on the interaction between silicate deposits and TBCs. Using a CO_2 laser and cooling air in a test facility, a controllable thermal gradient through the coating and underlying substrate is established for studying the interaction between two silicate compositions with state-of-the-art YSZ and bilayer $Gd_2Zr_2O_7$ (GZO)–YSZ coats grown by the EB-PVD method. Due to the high temperature environment and the thinness of the YSZ topcoat, the time needed for CMAS to penetrate the YSZ coatings is typically used to assess their resistance to CMAS infiltration [6,17,22,26,30–32]. Therefore, the understanding of the dynamic infiltration behavior of CMAS in YSZ topcoats is limited.

In comparison with the experimental investigation, there are fewer theoretical studies of CMAS infiltration in porous YSZ topcoats. Zhao et al. [10] and Naraparaju et al. [6] developed analytical expressions for penetration time of molten CMAS infiltration in isothermal YSZ topcoats, but did not consider the presence of the large temperature gradient and the temperature-dependent viscosity of the molten CMAS. Jackson et al. [33] developed a theoretical solution for CMAS penetration in the presence of a temperature gradient and temperature-dependent viscosity, but assumed a simplified temperature–viscosity relationship, as well as a stationary linear temperature distribution across the YSZ topcoat. In fact, molten CMAS, which has a higher thermal conductivity than gas, will raise the temperature of the infiltrated layer and subsequently favor further penetration by decreasing molten CMAS viscosity. The effect of the elevated temperature in the wetted region on the viscosity and infiltration has not been considered in the theoretical studies.

Microstructure optimization and use of multilayer structures are among various approaches attempted to reduce the deleterious effect of molten CMAS deposition. Naraparaju et al. [6] demonstrated in their study that a modified columnar morphology with more "feathery" features has better CMAS resistance than its counterpart at 1250°C and 1225°C. Yin et al. [23] designed an ideal theoretical microstructure consisting of columnar crystals that have feathery structures on their sides. Unfortunately, comprehensive understanding of the dynamics of CMAS infiltration in heterogeneous structures is limited due to the difficulty to measure infiltration rate at such high temperatures, the challenge of creating an equivalent temperature gradient across a thin layer, and the high cost associated with generation of YSZ topcoats of various microstructures. To the authors' best knowledge, the effect of multilayer structures of YSZ topcoats on CMAS infiltration has not been investigated theoretically. This study introduces an integrated model for CMAS infiltration in porous structures that incorporates heat transfer, liquid flow in unsaturated porous structures, and temperature-dependent viscosity. This model will be used to investigate the dependence of CMAS infiltration rate and depth on thermal conditions, CMAS compositions, microstructures, and multilayer structures. It is anticipated that quantitative information and advanced understanding of the infiltration dynamics obtained through the numerical study would benefit the development of an anti-CMAS infiltration solution through manipulation of temperature and microstructures.

II. Mathematical Models

Infiltration of molten CMAS in unsaturated porous YSZ topcoats involves two media separated by a moving wetting front: CMAS melt and turbine gas in the pores. It is assumed that the second fluid, the gas, is negligible with regard to its effect on the liquid flow, due to the disparate thermal and physical properties such as density and viscosity. Therefore, it is only necessary to model the liquid flow in the porous layer. Molten CMAS can be considered as a Newtonian liquid over the range of temperature considered in this study [35], and its densities indicate a variation of less than 3% over the temperature range of 1000°C–1400°C [36]. We also neglect the reactions of the molten CMAS with the YSZ material. Therefore, the mass conservation equation and the Darcy's equation for incompressible fluid flow in porous media are employed to describe the CMAS flow through the porous layer, which are as follows:

$$\nabla \cdot \boldsymbol{V}_p = 0 \tag{1}$$

$$\boldsymbol{V}_p = -\frac{K}{\mu(T)} \nabla P \tag{2}$$

where $\boldsymbol{u}_p$ is the average velocity of the fluid in the porous medium; K is the permeability of the porous medium; $\mu(T)$ is the CMAS viscosity, which is highly dependent on the temperature; and P is the pressure in the porous medium.

The level-set method is used to keep track of the wetting front of the liquid [37–39]. A color function c is defined to indicate the CMAS infiltrated region, where:

$$c = \begin{cases} 1, & \text{for region wetted by the molten CMAS} \\ 0, & \text{for dry porous structure} \end{cases} \tag{3}$$

The evolution of c's distribution over time during the infiltration process is prescribed by the transient advection equation:

$$\frac{\partial}{\partial t}(\varepsilon c) + \nabla \cdot (\boldsymbol{V}_p c) = 0 \tag{4}$$

where ε is the porosity.

The YSZ topcoat is subject to a large temperature gradient, in which the temperature at the top surface is high, but drops quickly across the thickness of the topcoat due to the low thermal conductivity of the YSZ porous layer. The molten CMAS infiltration enhances heat transfer from the top surface and elevates the temperature in the CMAS-infiltrated region. Given the highly temperature-dependent viscosity of CMAS, the effect of temperature elevation on the infiltration rate should be included in the model. In this study, heat transfer during CMAS infiltration is treated as a problem with two domains: one is the dry porous region; the other is the domain wetted by CMAS. In both regions, a local thermal dynamic equilibrium is assumed between the solid matrix and the CMAS/gas that fills the pores. In the wetted domain, there exists convection due to the CMAS flow in the pores. The thermal Péclet number compares the importance of the conduction with the convection heat transfer:

$$Pe = \frac{VL}{\alpha} \tag{5}$$

A typical maximum infiltration velocity of $V = 10\ \mu\text{m/s}$, a thickness of $L = 200\ \mu\text{m}$, and a thermal diffusivity of the molten CMAS of $\alpha = 1\text{e} - 6\ \text{m}^2/\text{s}$ result in a Péclet number $Pe = 0.002$. Such a low Péclet number illustrates that the convection of the molten CMAS in the porous structure plays a negligible role, and thus heat transfer in both regions is described by the volume-averaged heat conduction equation in porous media, which is expressed as follows:

$$\frac{\partial}{\partial t}[(\rho C_p)_{\text{eff}} T_p] = \nabla \cdot (k_{\text{eff}} \nabla T_p) \tag{6}$$

where k_{eff} and $(\rho C_p)_{\text{eff}}$ are the effective thermal conductivity and effective thermal capacity of the porous YSZ topcoat with molten

CMAS/gas in the pores, respectively, and T_p is the average temperature of the porous medium.

The melting temperatures of CMAS variants fall in the range between 1185°C and 1250°C [18,29,33,40], depending on their chemical compositions. Existing studies also indicate that phase transformation of CMAS occurs over a range of temperatures, and infiltration continues in this process. Jackson et al. [33,34] observed CMAS infiltration under temperatures below the melting point. To consider the worst scenario of CMAS infiltration, this study does not consider CMAS phase change during the infiltration process.

III. Problem Setup and Numerical Issues

We consider infiltration of a large amount of molten CMAS deposit on the turbine surface. The molten CMAS penetration and heat transfer across YSZ porous topcoats are assumed to be one-dimensional, as shown in Fig. 1, due to their typical thickness L in the range from 100 to 400 μm and the large area of CMAS deposition. It is also assumed that the molten CMAS temperature remains quasi-steady-state during the infiltration process, and that the infiltration depth is not limited by the CMAS volume on the surface. Before the CMAS infiltration, the YSZ topcoat is dry with $c = 0$, and at the top surface $z = 0$, the temperature is T_{top}. The bottom surface, $z = L$, is impermeable and the temperature is assumed constant at T_L. Both T_{top} and T_L are determined by the balance between the internal cooling in the turbine blade and the heating over the top surface. In this study, T_{top} and T_L are given values to assess the impact of turbine thermal conditions on CMAS infiltration. The initial temperature distribution in the porous layer is a linear distribution. At the top surface where $z = 0$, the color function is given as $c = 1$, representing full wetting. At the bottom surface where $z = L$, $dc/dz = 0$.

The absorption of the molten CMAS into the porous layer is mainly driven by the capillary pressure at the moving wetting front. At the microscale, the wetting front is a meniscus formed as the liquid penetrates the unsaturated pores. For a liquid with good wettability on the solid, the meniscus exhibits a concave shape, and the liquid is drawn into the porous structure due to surface tension. Otherwise, a nonwetting liquid–solid interaction yields a convex-shaped meniscus with a wetting force against the liquid advancement. The wetting interaction inside the porous medium is typically approximated as the capillary pressure at macroscale, which can be calculated using the Young–Laplace equation [41]:

$$P_c = -\frac{2\sigma \cos\theta_e}{r_c} \tag{7}$$

where P_c is the capillary pressure, σ is the surface tension of the liquid, θ_e is the static contact angle, and r_c is the effective radius of the capillaries or pores. Existing experimental studies show that the contact angle of CMAS on the YSZ topcoat is around 13 deg [25,42], with noticeable variations due to temperature and surface roughness. As it is most commonly treated as completely wetting [6,10,18,32], $\theta_e = 0$ deg is adopted in this study. The resulting capillary pressure will be negative and will pull the liquid into the dry medium. The resulting boundary condition at the moving wetting front $z = h_p(t)$ *is* $P = P_c$. In the YSZ topcoat, the small pore sizes, high surface tension, and good wettability result in a very high capillary pressure at the wetting front. The top surface $z = 0$ is then treated as a constant pressure inlet, that is, $P = 0$. In addition, the continuities in both temperature and heat flux are enforced at the wetting front that separates the wetted and dry regions having different thermal properties.

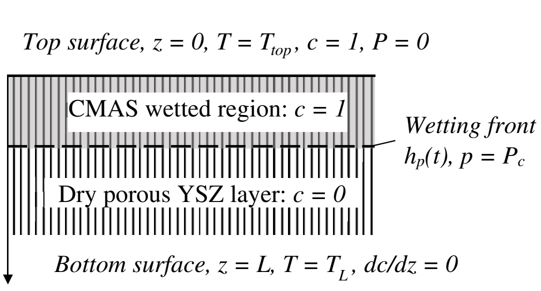

Fig. 1 Problem setup and boundary conditions.

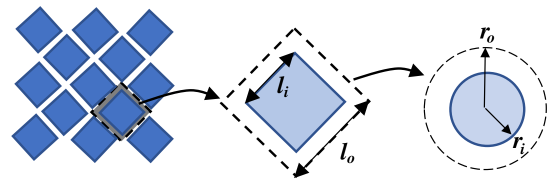

Fig. 2 Columnar structure and parameters for permeability calculation.

The hydraulic permeability of the YSZ topcoat is determined by the porosity, pore size, and tortuosity of the pores of the microstructure. A YSZ porous layer formed via EB-PVD consists of parallel columns with roughly quadrilateral cross sections that grow perpendicular to the substrate surface [4,6]. Unfortunately, information on permeability and effective capillary pressure on YSZ porous layers is limited. As schematically illustrated in Fig. 2, Naraparaju et al. [6] approximated the columns as solid cylinders, and employed a correlation developed by Dvorkin [43] for a porous medium consisting of the annular gaps around cylindrical solid columns:

$$K = \frac{\varepsilon D_o^2}{32\tau^2}\left[1 + \left(\frac{D_i}{D_o}\right)^2 + \left(1 - \left(\frac{D_i}{D_o}\right)^2\right)\frac{1}{\ln(D_i/D_o)}\right] \tag{8}$$

where D_o is the outer diameter of the annular gap, and D_i is the column diameter. The TBC topcoats' quadrilateral columns are approximated to the round columns by setting their perimeters equal to each other:

$$D_i = \frac{4l_i}{\pi}, \quad \text{and} \quad D_o = \frac{4l_o}{\pi} \tag{9}$$

For liquid infiltration in a very narrow annular gap, the effective capillary radius used in Eq. (7) can be approximated as half of the gap width, which is

$$r_c = \frac{D_o - D_i}{2} \tag{10}$$

The permeability calculated from Eq. (8) was used in the theoretical calculation of CMAS infiltration under isothermal conditions [32]. Despite the bold simplification of the porous structure, the predicted infiltration rate was consistent with the experimental observation for isothermal tests [32]. Therefore, these relations are adopted in this study. We test topcoat microstructures with two column diameters but the same porosity of 0.15. The structure with finer columns has a higher columnar density per unit area and narrower pores.

Pore tortuosity is another important microstructural characteristic that varies considerably, depending on the process parameters of the growth process. A basic approximation of a set of parallel vertical columns would result in a tortuosity $\tau = 1$. Due to the crystal growth process used, columns may grow at an angle, grow larger or smaller in a cross-sectional area, join other columns, and/or branch off to produce smaller columns [6]. These microstructure variances contribute to the variability of the tortuosity [23,32–34,42]. In this study, a tortuosity of 7 is used.

Effective thermal conductivity in YSZ topcoats is a topic of extensive study, due to its central importance to TBC performance. Rayleigh's model [44] that emphasizes conductivity in the axial direction of cylindrical pores is adopted in this study for the wetted region, as it is a suitable approximation for the column structure of EB-PVD top layers. The effective thermal conductivities in both regions are expressed as

$$k_{\mathrm{eff}} = \begin{cases} k_m\left(1 + \varepsilon\left(\dfrac{k_f}{k_m} - 1\right)\right), & \text{infiltrated by CMAS} \\ k_{\mathrm{eff,\ unsaturated}}, & \text{occupied by gas phase} \end{cases} \tag{11}$$

where k_{eff} is the effective thermal conductivity with the porosity ε, k_m is the thermal conductivity of the matrix material, and k_f is the infiltrating fluid thermal conductivity. The YSZ and CMAS thermal conductivities in this study are given in Table 1. The experimentally measured thermal conductivity of dry porous YSZ topcoats formed by EB-PVD ranges from $1.25\ \mathrm{W/(m\cdot K)}$ to $1.6\ \mathrm{W/(m\cdot K)}$, with the lowest thermal conductivities corresponding to the finest microstructures [45]. For this study, we use an intermediate thermal conductivity of $1.4\ \mathrm{W/(m\cdot K)}$ for the unsaturated porous layer.

The effective density and specific heat of the porous layer is determined as

$$(\rho C_p)_{\mathrm{eff}} = \begin{cases} \varepsilon(\rho C_p)_{\mathrm{CMAS}} + (1-\varepsilon)(\rho C_p)_{\mathrm{solid}}, & \text{infiltrated by CMAS} \\ \varepsilon(\rho C_p)_{\mathrm{gas}} + (1-\varepsilon)(\rho C_p)_{\mathrm{solid}}, & \text{occupied by gas phase} \end{cases} \tag{12}$$

where C_p is the specific heat.

Turbine inlet temperatures for current gas turbines can exceed 1400°C, whereas turbine blades, with a service temperature ~750°C, should be kept below 1000°C [46,47]. A typical CMAS's viscosity varies in multiple orders of magnitude over that temperature range. Several models have been proposed for the molten silicate viscosity–temperature relationship, including the Iida model [48], the Vogel–Fulcher–Tamman equation, and the more recent model developed by Giordano et al. [35]. This study utilizes the viscosity–temperature relationship by Giordano et al. for its correlation with recent experimental data and for its flexibility with regard to CMAS compositions. It has been used to model CMAS viscosity for desert sand [10,33,34], volcanic ash [22], and other CMAS variants [32,49]. It is expressed as [35]

$$\log \mu = A + \frac{B}{T - C} \tag{13}$$

where A, B, and C are constants. The constants B and C relate to silicate composition through contemporary experimental viscosity data, whereas A sets the high-temperature viscosity limit, which is found to be -4.55 ± 0.21 [35]. This study considers a commonly used CMAS formulation based on deposits of sand particles found on turbine components that operated in desert environments [17]. It has a CMAS composition of CaO: 33, MgO: 9, Al_2O_3:15, and SiO_2:45 mol%, with $B = 4708$ and $C = 680.8$. This viscosity–temperature relationship has been used in the studies by Jackson et al. [33,34] and Zhao et al. [10].

The set of equations for CMAS infiltration and heat transfer in the porous YSZ topcoat is solved numerically via an in-house developed code based on the finite volume method. The combined Darcy's law and the mass conservation equation are solved over the wetted region, whereas the heat transfer equation is solved over the entire domain with heterogeneous thermal properties. The wetting front is tracked with the level-set method. Second-order space discretization is used for the pressure and the heat conduction equations. Advection of the level set is calculated using a first-order upwind scheme. The set of transient equations are highly coupled and highly nonlinear, so they are solved using an implicit iterative scheme. At each time step, the pressure and velocity are obtained first to allow the level-set equation to be solved and to update the location of the wetting front. Based on the updated wetting front location, the heat transfer equation is then solved to determine the temperature in both wetted and unsaturated regions. The viscosity is then updated with the new temperature, and the pressure and velocity fields are recalculated. The iteration process is repeated until convergence is achieved, indicated by the residual of the color function:

$$\mathrm{res}_{\mathrm{color}} = \| c^{j+1} - c^{j} \| < \mathrm{tol} \tag{14}$$

where an absolute tolerance $\mathrm{tol} = 1E - 8$ is used. The mesh size and time step are 1 μm and 1 ms, respectively. Mesh and time step dependency studies were carried out with 50% reductions in both, leading to the total infiltration time varying by less than 0.1%. The numerical model has been verified using the theoretical solutions of CMAS infiltration in porous structures under various thermal conditions, shown in the Appendix. Material properties and geometrical parameters for all cases are given in Table 1.

IV. Results and Discussion

Numerical simulation has been performed to understand the dynamic behavior of CMAS infiltration in the YSZ topcoat in the presence of a large temperature gradient. Of special interest are the effects of the enhanced heat transfer by CMAS infiltration and the CMAS penetration through YSZ topcoats of various microstructures. We also simulated infiltration under various thermal conditions and CMAS compositions. As the infiltration rate close to the bottom surface is quite low, we only present infiltration up to the top 200 μm.

A. Infiltration Through Homogeneous YSZ Porous Topcoats

We simulated a baseline case using the CMAS and YSZ properties and parameters given in Tables 1 and 2. Figures 3a–3c show the pressure, the temperature, and the CMAS viscosity variations over depth z, respectively, at various infiltration times. The overall pressure gradient decreases with time, and the pressure distribution becomes more nonlinear toward the end of the infiltration process. Figure 3b shows a decreasing temperature from the top-to-bottom surfaces of the topcoat, with the temperature gradient in the CMAS-wetted region smaller than in the dry region, due to the higher thermal conductivity. Also, the temperature in the wetted region is above that value before the CMAS infiltration. As the wetting front advances, the molten CMAS viscosity increases from 18 $\mathrm{Pa\cdot s}$ at 100 μm to nearly

Table 1 Material properties and simulation parameters[a]

Variable	Symbol	Value
CMAS density	ρ_L	$2690\ \mathrm{kg/m^3}$ [20]
CMAS dynamic viscosity	μ	5.31–178 $\mathrm{Pa\cdot s}$ over a temperature range of 1100°C–1300°C
CMAS thermal conductivity	k_f	$3\ \mathrm{W/(m\cdot K)}$ [34]
Molten CMAS heat capacity	$C_{p,L}$	$900\ \mathrm{J/(kg\cdot K)}$ (at 70°C) [50]
Molten CMAS surface tension	σ	$0.4\ \mathrm{Pa\cdot m}$ [10,18,51]
Viscosity parameters for sand-derived CMAS	$[A, B, C]$	−4.55, 4708, 680.8
YSZ bulk thermal conductivity	k_m	$2.64\ \mathrm{W/(m\cdot K)}$
YSZ heat capacity	$C_{p,M}$	$475\ \mathrm{J/(kg\cdot K)}$ (at 70°C) [50]
Porous topcoat	k_{eff}	$1.4\ \mathrm{W/(m\cdot K)}$ (Unsaturated) [45]
Thermal conductivity		$2.7\ \mathrm{W/(m\cdot K)}$ (Saturated) (Rayleigh equation)
YSZ layer porosity	ε	0.15
Tortuosity of YSZ topcoats	τ	7
YSZ layer thickness	L	300 μm

[a]CMAS in this study, unless specified, refers to the most studied turbine deposit of sand particles from aeroengines operating in a desert environment.

Table 2 Structural and operational parameters of YSZ porous topcoats

Square column side length, l_i	Characteristic length of the column, D_i	Outer diameter of the annular gap, D_o	Effective capillary radius, r_c	Permeability, K	Capillary pressure, P_c	Bottom and top surface temperature of the YSZ topcoat, T_L and T_{top}
10 μm	12.73 μm	14.43 μm	0.85 μm	1.83E−16 m^2	−945 kPa	1100°C and 1250°C

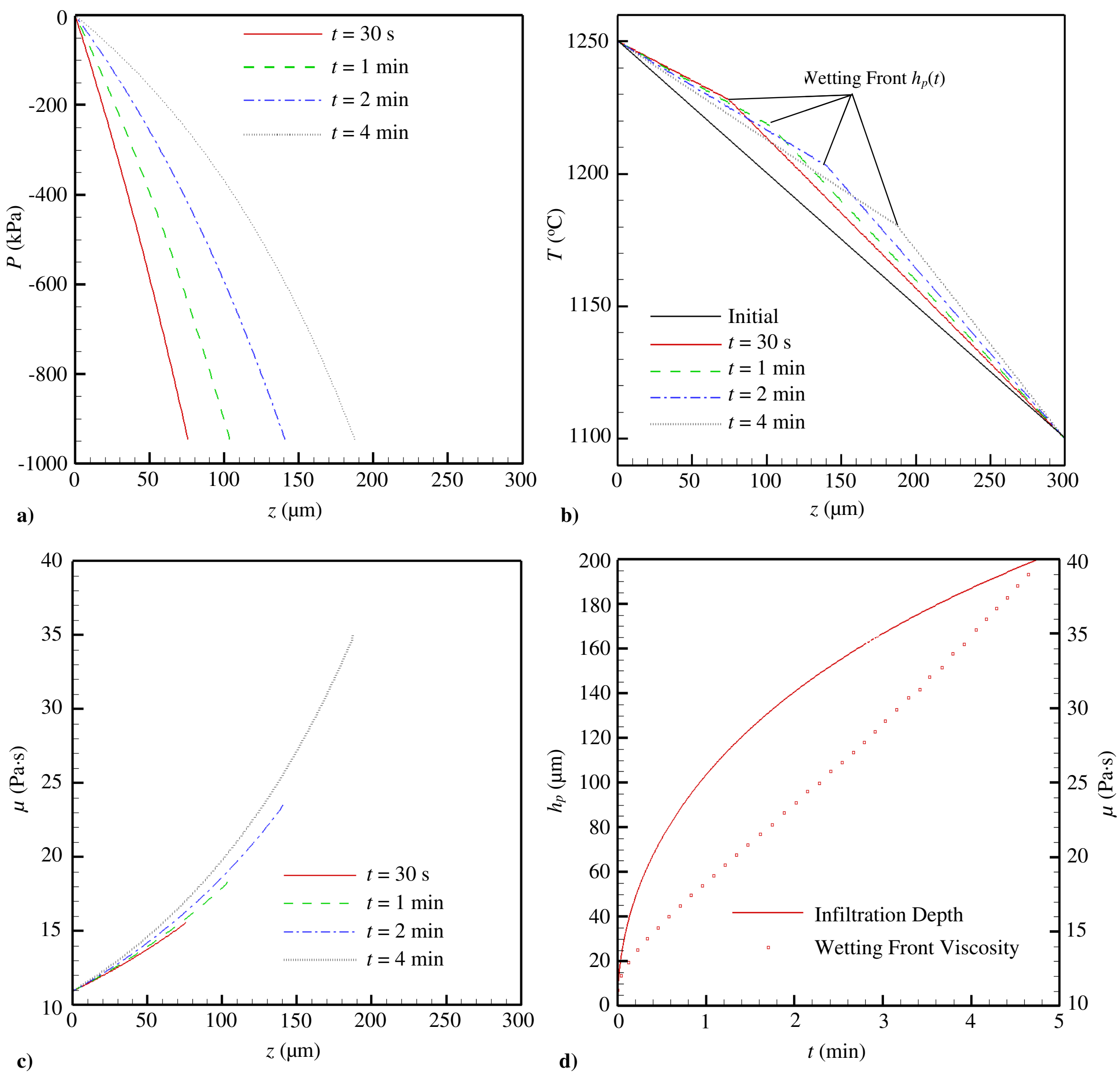

Fig. 3 CMAS infiltration through a homogeneous YSZ topcoat: a) pressure vs depth in wetted region at different times, b) temperature distributions at different times, c) viscosity vs depth in wetted region at different times, and d) wetting front position.

40 Pa · s at 200 μm depth, as shown in Fig. 3c. Figure 3d shows the CMAS infiltration depth and the viscosity at the wetting front over time, respectively. The wetting front location exhibits a logarithmic slowdown over the course of the infiltration process. The infiltration velocity reduces from an average of 3.94 μm/s over the first 50 μm to 0.34 μm/s just over 150–200 μm. As a result, although infiltration to 200 μm completes in about 4 min 45 s, half of the sorption occurs in the first 55 s of the process.

The nonlinear dynamics of the CMAS infiltration, demonstrated by the nonconstant pressure gradient, stems from the large temperature drop across the topcoat and the temperature-dependent viscosity. During the early stage of the infiltration, the CMAS viscosity is low, due to the high local temperature near the top surface, whereas the pressure gradient, which is on the order of $P_c/h_p(t)$, is high, due to a short penetration depth $h_p(t)$. The immense pressure gradient and low viscosity result in expedient infiltration near the top surface. This behavior must be considered in the development of a strategy to mitigate CMAS infiltration.

Practically, YSZ topcoats have a low thermal conductivity to protect the base material. In the wetted region, the observed temperature elevation from the initial temperature is the result of the enhanced heat transfer by the more thermally conductive CMAS. To understand how the temperature elevation by the CMAS infiltration affects the infiltration rate, we simulated the CMAS infiltration based on the initial linear temperature distribution, as displayed in Fig. 3b. The infiltration of CMAS over time with or without consideration of heat transfer enhancement is compared in Fig. 4. Although the local temperature elevations from without CMAS enhancement to with CMAS enhancement are only 1.6% and 2%, respectively, for the wetting fronts at 100 and 200 μm, the CMAS infiltration shortens the time taken to reach these locations by 11.3% and 15%, respectively. Overall, neglecting enhanced heat transfer by CMAS infiltration using an approximated linear distribution over the topcoat underestimates the infiltration rate and time. Neglecting CMAS heat transfer enhancement will cause an additional underestimation of the heat transfer rate to the substrate. When a wetted region is 100 μm in

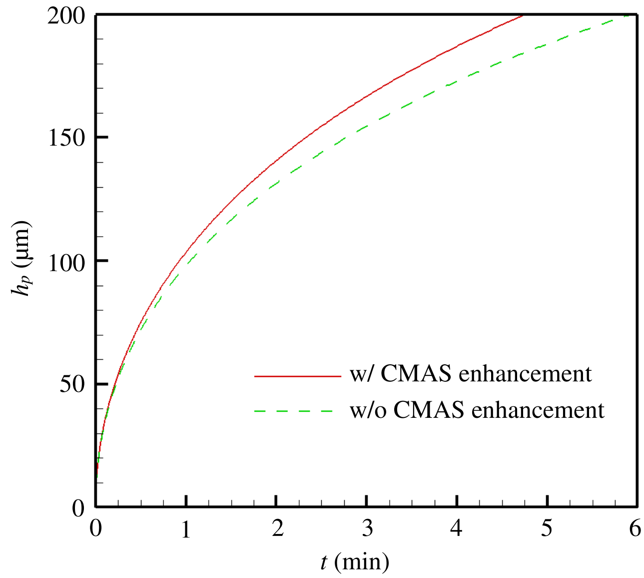

Fig. 4 Infiltration depth vs time with/without consideration of CMAS-enhanced thermal conductivity.

depth, the heat flux through the porous medium is 833 kW/m^2, in comparison with a flux of 700 kW/m^2 without considering the reduced heat transfer resistance. It is also observed in Fig. 3b that although CMAS infiltration alters the initial temperature distribution across the topcoat, the temperature profile in each region, wetted or dry, retains linearity, indicating a quasi-steady-state heat transfer in the topcoat. With this information, a one-dimensional thermal resistance analysis method can be used to find out the temperature distribution, thus greatly reducing the computational cost.

B. Effect of Thermal Conditions on CMAS Infiltration

An important path to a better gas turbine efficiency is higher turbine inlet temperatures. However, it is limited by the turbine materials' thermal limits and cooling capabilities. Different systems will have differing temperature gradients, due to the particular inlet temperatures and cooling conditions set by the turbine operator. It has been found that a 25°C increase in turbine blade temperature can reduce the lifetime of the turbine blade by a factor of 2 [52,53]. We conducted an investigation into the effects of thermal boundary conditions on CMAS infiltration using the properties of the molten CMAS and YSZ topcoats given in Tables 1 and 2. The top and bottom temperatures of the topcoats are given in Table 3.

We first examined the effect of the bottom surface temperature while the top surface temperature is maintained at 1250°C. As shown in Fig. 5a, lowering the bottom temperature by 50°C does not significantly affect the infiltration rate in the top layer up to 80 μm. Over the section 100–200 μm, the average infiltration rate for the colder bottom temperature case is 21.6% slower. On the other hand, both the total and initial infiltration rates are very sensitive to the top surface temperatures, as a higher top surface temperature significantly lowers the viscosity for initial infiltration when the pressure gradient is higher. The average infiltration velocity for the case with a top surface temperature of 1300°C over the top 50 μm is 8 $\mu m/s$, reflecting a roughly 103% increase compared with the case with 1250°C. The viscosity of the CMAS at the wetting front during infiltration is displayed in Fig. 5b.

Table 3 Temperature boundary conditions

T_{top} (°C)	T_L (°C)
1300	1100
1250	1100
1250	1050

C. Effect of CMAS Compositions on Infiltration

The CMAS composition has arguably the strongest influence on viscosity, apart from temperature. The varying compositions of volcano ash and sand present different levels of threat to high-temperature aerospace gas turbines operating in different environments. The molten CMAS properties presented in Table 1 correspond to CMAS formulations taken from deposits in real turbines. These turbines operated in sandy environments, so we term this formulation "sand-derived CMAS." In this study, we further investigated infiltration of CMAS from Eyjafjallajökull volcano ash (VA) and Sakurajima VA in the topcoat. Their CMAS compositions are compared in Table 4 with the corresponding temperature-dependent viscosity parameters of Eq. (13) given in Table 5. The temperatures at the top and bottom surfaces of the YSZ topcoat are 1250°C and 1100°C, respectively. The YSZ properties can be found in Tables 1 and 2.

Although the three CMAS compositions exhibit similar infiltration dynamics, the infiltration rate differs largely, due to the viscosity–temperature relationship. Transient infiltration behavior for the three cases is compared in Fig. 6, with associated infiltration times to 50 μm and 100 μm depth, shown in Table 5. The sand-derived CMAS has the lowest viscosity and shortest infiltration time at nearly 4 min, and the Eyjafjallajökull VA has the highest viscosity at any temperature and the longest infiltration time. The time taken by the molten sand-derived CMAS to wet the top 200 μm of the TBC is the same as that taken by the Eyjafjallajökull VA to wet the top 100 μm of the topcoat. The Sakurajima VA is only slightly faster. Information on CMAS infiltration behavior between volcano ash and sand is crucial to assess the risk encountered by the aero gas turbines that may operate in unexpected environments and locations. Also, quantitative understanding also helps to avoid increased cost due to having a too stringent infiltration mitigation strategy.

D. Effect of YSZ Microstructures on CMAS Infiltration

YSZ topcoats grown through EB-PVD possess columnar microstructures with various porosities (0.1–0.4) [33,34,45], pore sizes (0.1–2.3 μm) [6,53], and crystal column sizes (1–20 μm) [6,53]. Practically, the process parameters used in the EB-PVD process can vary the EB-PVD microstructure from fine to coarse columnar structures [54]. However, to what extent the column size affects infiltration remains unclear. In this study, we compared infiltration through microstructures with two different column characteristic lengths, 10 and 5 μm, assuming the same overall porosity of 0.15. The intercolumnar gaps scale down with the column diameter to maintain the same porosity. For parallel columnar structures, thermophysical properties are functions of porosity only, and thus remained unchanged. The properties of these two microstructures are given in Table 6. The top and bottom surface temperatures are 1250°C and 1100°C, respectively, and the CMAS composition is based on sand, with properties given in Table 1.

Figure 7 shows that reduction in column diameter has a noticeably slower infiltration rate. The average infiltration rate over the top 50 μm is 1.96 $\mu m/s$ for the topcoat with finer columns, which is 50% slower than the other over the same depth. When porosity remains unchanged, the decreased pore size has two opposing effects on infiltration: it reduces permeability and creates more resistance to flow while it enhances capillary pressure, drawing the molten CMAS into the porous medium via the wetting interaction. The resistance to infiltration overpowers the enhanced capillary pressure. Therefore, creating microstructures with fine columns and fine pores offers a solution to reduce the CMAS infiltration rate.

E. CMAS Infiltration into YSZ Topcoats of Heterogeneous Column Structures

Multilayer topcoat structures give the material designer/engineer a greater ability to add functionality such as corrosion protection and CMAS infiltration mitigation through decreased wettability and/or permeability [7,55]. The microstructure properties, thickness, and arrangement of the multilayer can be tailored to mitigate CMAS infiltration without significantly compromising the overall thermomechanical properties. It is critical to understand the infiltration

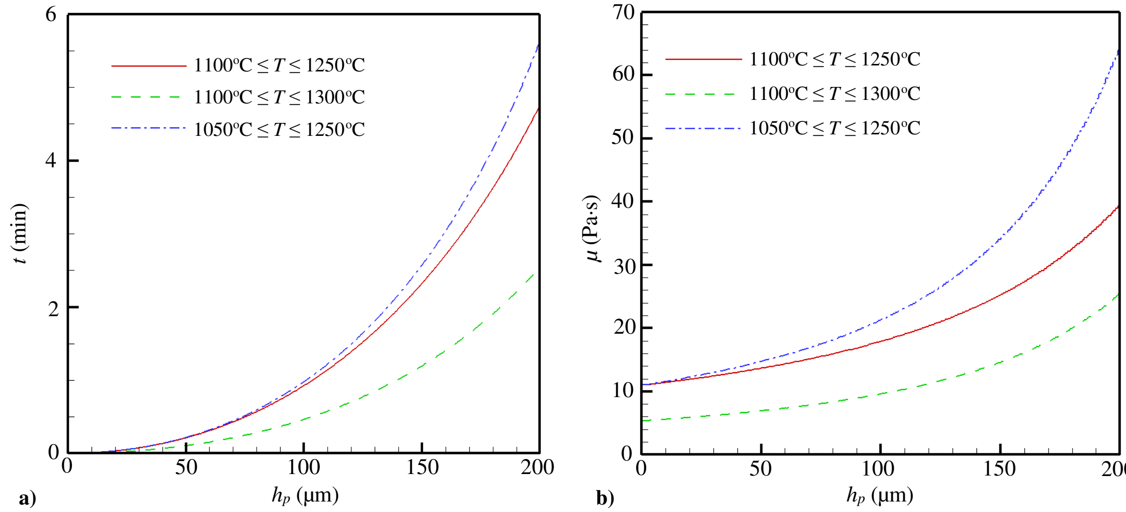

Fig. 5 a) Infiltration time vs wetting front location for various top and bottom temperatures, and b) wetting front viscosity vs wetting front location.

Table 4 CMAS Compositions for viscosity investigation (mol %)[a]

Case	CaO	MgO	FeO	Al_2O_3	SiO_2	TiO_2	Na_2O	K_2O	MnO	Ta_2O_5
Sand-derived CMAS	33	9	0	13	45	0	0	0	0	0
Eyjafjallajökull[b] VA	12.5	6.1	17.6	7.4	49.7	4.3	2.0	0.4	0	0
Sakurajima[c] VA	10.34	3.04	13.11	12.48	54.9	0.08	4.25	1.72	0.05	0.03

[a]VA compositions vary in literature. Superscripts denote sources for each formulation:
[b][22],
[c][23].

Table 5 Parameters for different CMAS compositions and viscosity treatments

Case	B	C	μ at 1250°C (Pa · s)	μ at 1173°C (Pa · s)	Infiltration time, 50 μm (s)	Infiltration time, 100 μm (s)
Sand-derived CMAS	4708	680.8	11	40	13	56
Eyjafjallajökull VA	5478	647.2	51	202	59	260
Sakurajima VA	5816	585.2	45	160	52	228

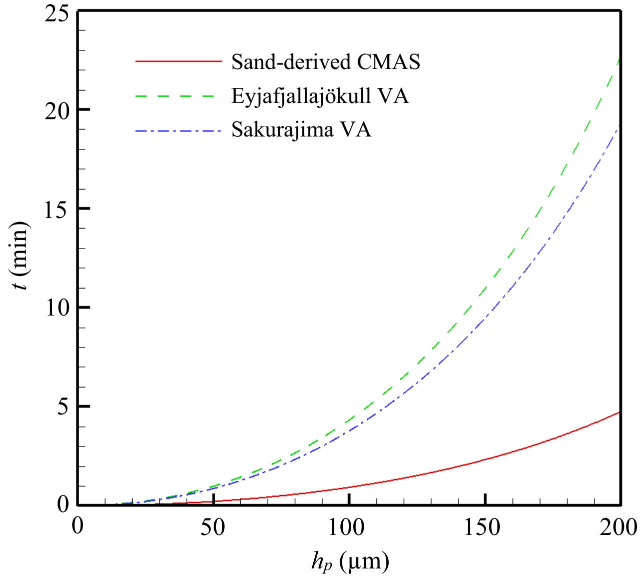

Fig. 6 Infiltration time vs depth for various CMAS compositions.

behavior in such kinds of hybrid structure systems to achieve an efficient CMAS-resistant outcome.

We first studied infiltration through bilayers, as shown in Fig. 8a, which consist of the two different columnar structures studied in Sec. IV.C. The top layer of the hybrid structure has a finer column size (6.37 μm in diameter) and narrower pores that have demonstrated a higher resistance to CMAS infiltration; the remaining thickness of the topcoat has the larger column diameter of 12.73 μm with a larger pore size. Bilayer structures with two top-layer thicknesses, $L_0 = 30$ and 60 μm, were used. The transient wetting front locations over time for the bilayer structures are compared with a single layer having the homogeneous fine columns of 6.37 μm in diameter. To illustrate the structural effect only, the three structures have the same total thickness, porosity, and thermal properties. Thermal boundary conditions

Table 6 Properties of columnar microstructures with different column sizes

Case	l_i (μm)	D_o (μm)	D_i (μm)	r_c (μm)	K (m^2)	P_c (kPa)
Coarse column	10	14.43	12.73	0.85	1.83E-16	−945.0
Fine column	5	7.21	6.37	0.42	4.57E-17	−1890.1

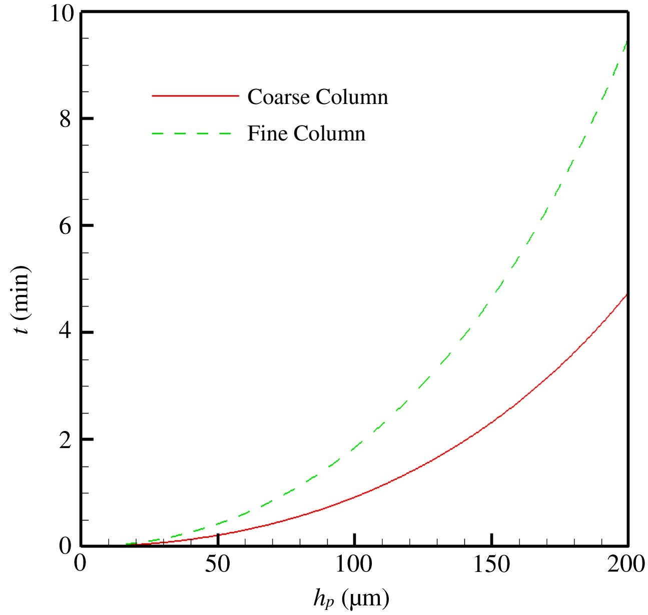

Fig. 7 Infiltration time vs depth for microstructures with coarse and fine columns.

are 1250°C at the top surface and 1100°C at the bottom surface, and the CMAS properties are based on sand, as given in Table 1.

The CMAS penetration depths vs time for the three structures are presented in Fig. 9a, and the pressure profiles for the bilayer and homogeneous structures are compared at an infiltration depth of 100 μm in Fig. 9b. The behavior of the bilayer structures is more interesting when compared with the single layer of fine columns. As compared in Fig. 10, the three structures share the same infiltration behavior over the first 30 μm due to identical microstructures. Between 30 and 60 μm, interestingly, the thin-top bilayer structure ($L_0 = 30$ μm) demonstrates a slower penetration than the other two. However, beyond 60 μm, the thick-top layer structure ($L_0 = 60$ μm) exhibits the best CMAS infiltration resistance up to 200 μm, even better than the fine column single layer.

Although the homogeneous layer having the fine column structure is more resistant to infiltration than the coarse one, the bilayer structures combining both fine and coarse column sizes demonstrate a more effective resistance to infiltration. Such a bilayer microstructure mitigates infiltration in two ways: the fine column top layer adds extra resistance to infiltration, and the large pore size of the bottom layer constrains the capillary pressure at the wetting front. The thicker the fine-column top layer is, the greater the pressure head loss across it is, as shown in Fig. 9b. When the wetting front enters the coarse layer from the fine column layer, the flow slows down considerably, due to the lower capillary pressure and the top layer's lower permeability.

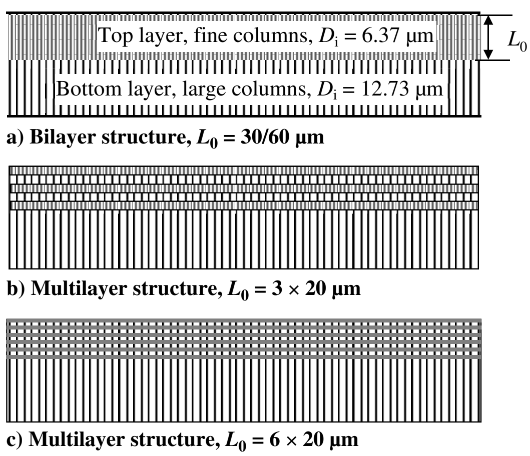

Fig. 8 a) Bilayer, and b, c) multilayer TBC structures. Bilayer/multilayer structures have the same total thickness as the single-layer topcoats.

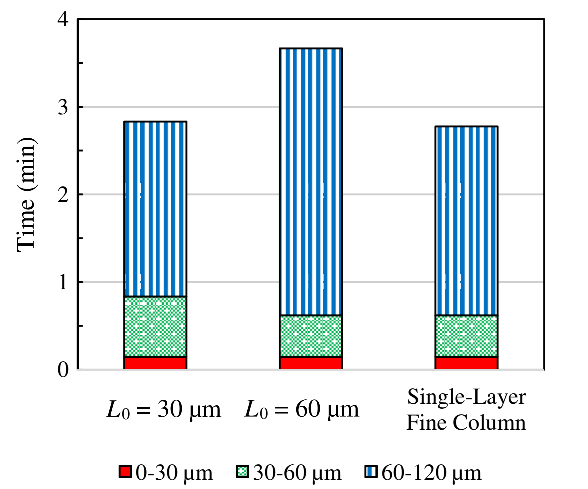

Fig. 10 Infiltration times to reach 30, 60, and 120 μm depth by fine-column single-layer and bilayer topcoats.

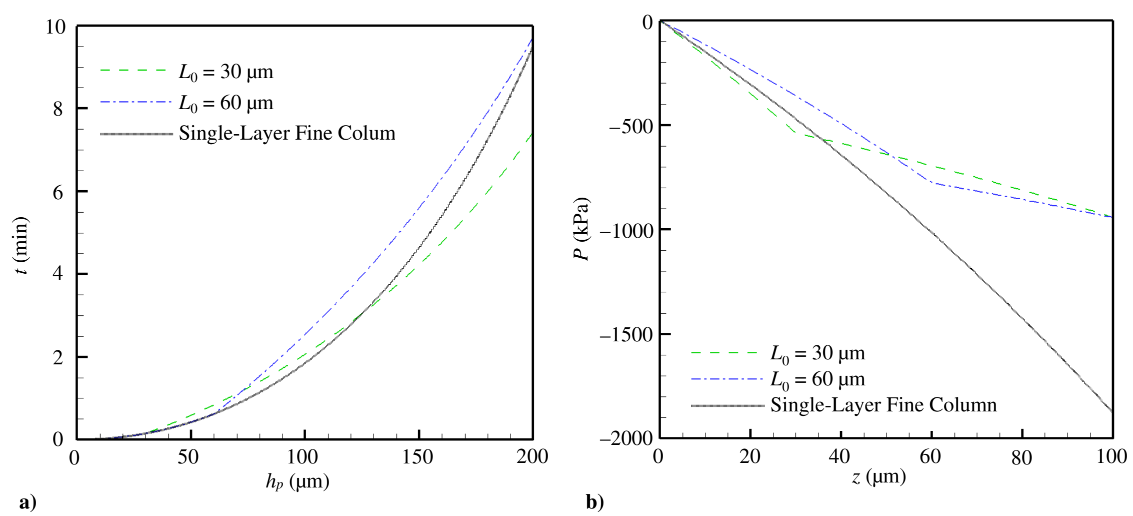

Fig. 9 a) Comparison of infiltration time vs depth for bilayer and single-layer structures, and b) pressure distribution in wetted depth of 100 μm.

For infiltration between 30 and 60 μm, the thin-top bilayer ($L_0 = 30$ μm) structure has the combined infiltration resistance and low capillary pressure, which explains the longer penetration time than other structures. Beyond 60 μm, the thick-top bilayer ($L_0 = 60$ μm) offers a higher hydraulic resistance than the thin-top layer, and a lower capillary pressure than the single layer, resulting in the slowest infiltration over this range. Given that infiltration is fastest near the hot surface of YSZ topcoats, using heterogeneous microstructures that take advantage of both infiltration resistance and reduced capillary pressure presents a possible path for CMAS infiltration mitigation.

We also compared the thick-top bilayer structure with two multilayer structures with alternating fine and coarse columns. As displayed in Figs. 8b and 8c, respectively, one has six layers of fine-column microstructure with a thickness of 10 μm, each embedded 10 μm apart in the regular structures, and the other has three layers of 20 μm layers, embedded 20 μm apart. In addition, all structures in Fig. 8 have the same porosity and the same topcoat thickness of 300 μm. Molten CMAS properties and thermal conditions remain unchanged from the bilayer simulation. The infiltration dynamics for the bilayer and alternating layer structures are compared in Fig. 11. It shows that infiltration in the thin multilayer structure (6×10 μm) is the slowest to reach the 20 μm infiltration depth, whereas the medium multilayer structure (3×20 μm) yields the slowest penetration up to the top 55 μm thickness. Most interestingly, infiltration in the thin multilayer topcoat is slower to reach 55 μm than the bilayer structure. Again, the slower penetration in the alternating multilayer structures during the early stage can be explained by the combined reduced capillary pressure and elevated resistance to infiltration. By reducing the thickness of each layer and increasing the number of layers, delayed infiltration starts sooner and lasts over a longer period of time compared to the corresponding bilayer structure.

This understanding of the infiltration behavior through an alternating multilayer structure is important for the development of alternating YSZ and GZO in multilayer structures [55]. GZO is a promising antiinfiltration material because of its low thermal conductivity and reactivity with CMAS to block further penetration. However, as GZO is also permeable, it is critical that the infiltration time across the GZO layer is sufficiently long for chemical reactions to complete and block further infiltration. The alternating multilayer structures offer a solution that could extend the penetration time within a limited depth from the top surface and allow more time for thermochemical reactions to occur.

One limitation of this study is the simplified column structures for evaluation of the hydraulic permeability and capillary pressure, due to the scarcity of the transport properties of YSZ topcoats grown by the EB-PVD method. Sophisticated structures such as smaller columns protruding from the main columns at an angle are considered by an estimated constant tortuosity. Additionally, the assumption of constant porosity for the heterogeneous structures is a simplification. However, the mechanistic understanding of CMAS infiltration behavior through a heterogeneous topcoat is still valuable for the development of gradient materials and multilayer structures to inhibit infiltration. In addition to properties, only infiltration is concerned in this study. Other factors such as thermomechanical properties and interface strength should also be considered when designing gradient structures for the YSZ topcoat of thermal engines. The numerical study of CMAS infiltration will continue with more realistic properties and structures of the topcoat. Phase change and chemical reactions in the YSZ material should be included in the future study to have a better understanding of the infiltration dynamics.

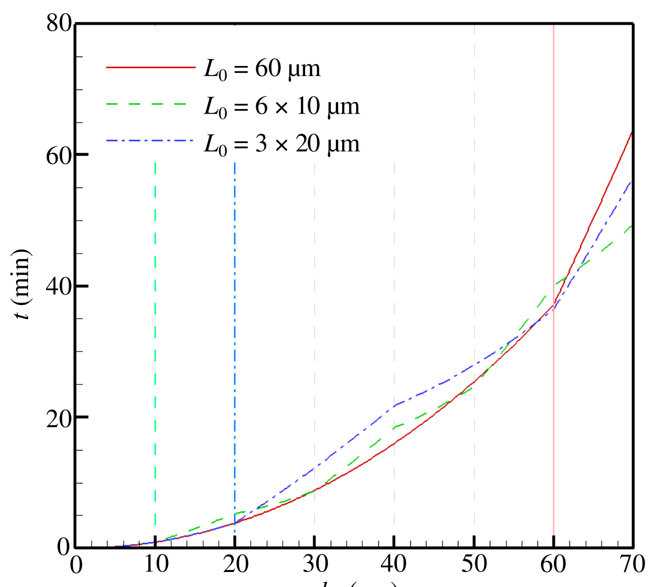

Fig. 11 Comparison of infiltration time vs depth for bilayer and multilayer structures with same fine-column total thickness (60 μm).

V. Conclusions

This study introduces an integrated model, incorporating heat transfer, liquid flow in unsaturated porous structures, and temperature-dependent viscosities to study CMAS infiltration through thermal barrier coatings with different CMAS compositions, temperature gradients across the topcoat, and various coating microstructures. CMAS infiltration exhibits nonlinear dynamics with fast infiltration at the earlier stage. Infiltration analysis may be simplified by neglecting the CMAS's influence on the porous medium's conductivity. However, the resulting approximated linear distribution over the topcoat underestimates the infiltration rate. It is also observed that although CMAS infiltration causes a lower temperature gradient in the wetted region than that in the dry region, the temperature profile in each of the regions retains linearity, indicating a quasi-steady-state heat transfer in the topcoat throughout the infiltration. Additionally, both the total and initial infiltration rates are very sensitive to the top surface temperatures, but the effect of the bottom surface temperature is only important in the later infiltration stage. For columnar porous structures of an identical porosity, the one with fine columns and narrow pores exhibits more resistance to CMAS infiltration. Bilayer or multilayer structures consisting of different column and pore sizes used in this study have the combined advantage of an increased hydraulic resistance to infiltration and a low capillary pressure. As a result, they have slower infiltration rates over intermediate lengths. Such heterogeneous structures can be used to delay infiltration at the early stage by manipulating the layer thickness and arrangement. It is anticipated that the quantitative information and the advanced understanding obtained through the theoretical study would benefit the development of anti-CMAS infiltration solutions through manipulation of temperature and microstructure.

Appendix

For one-dimensional infiltration of a liquid with a constant viscosity into a homogeneous porous medium, the analytical can be derived by solving Eqs. (A1) and (A2). For the boundary conditions of $z = 0$, 9
$P = 0$, and $z = h(t)$, $P = P_c$, the penetration depth is expressed as [6,10]

$$h(t) = \sqrt{-\frac{2KP_c}{\varepsilon\mu}t} \tag{A1}$$

Using the properties given in Table 6, the numerical and analytical solutions are compared in Fig. A1a. Total infiltration times differ by less than 0.1%.

We also tested the infiltration of CMAS, whose viscosity varies with the position z in the porous medium exponentially, which is

$$\mu(z) = Ce^{Az} \tag{A2}$$

where $z = 0$ coincides with the top surface of the porous layer. The constant C and A values used in the test were based on a viscosity–temperature relationship of CMAS infiltrating a 200 μm

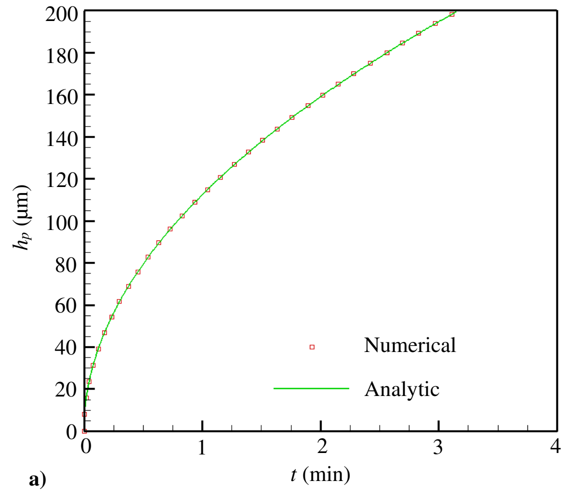

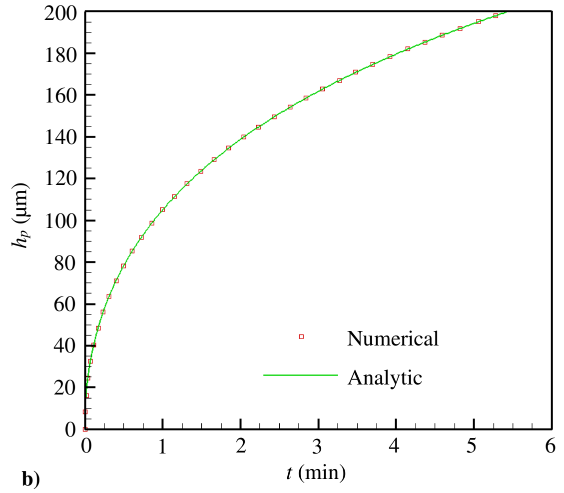

Fig. A1 Comparison of theoretical and numerical solutions with a) constant viscosity, and b) exponentially varying viscosity.

Table A1 One-dimensional infiltration parameters for constant viscosity case

K (m^2)	P_c (kPa)	μ (Pa · s)
1.829E-16	−945	10.94

porous layer whose top and bottom temperatures are 1250°C and 1150°C, respectively. The exponential variation of the viscosity with position corresponds to a linear temperature distribution in the porous layer.

The theoretical relationship between the infiltration time t and the penetration depth $h(t)$ is [38]

$$t = \frac{C\varepsilon}{KAP_c}\left(\frac{e^h - 1}{A} - h\right) \tag{A3}$$

The analytical and numerical solutions for $C = 8.561$ and $A = 10020$ are compared in Fig. A1b. The time needed to penetration top 200 μm obtained by the analytical and numerical solutions also differ by 0.1%.

Acknowledgment

This research was supported in part by a National Science Foundation research grant CBET-1705538.

References

[1] Liebert, C. H., and Miller, R. A., "Ceramic Thermal Barrier Coatings," *Industrial & Engineering Chemistry Product Research and Development*, Vol. 23, No. 3, 1984, pp. 344–349. https://doi.org/10.1021/i300015a004

[2] Jones, R. L., Reidy, R. F., and Mess, D., "Scandia, Yttria-Stabilized Zirconia for Thermal Barrier Coatings," *Surface and Coatings Technology*, Vol. 82, Nos. 1–2, 1996, pp. 70–76. https://doi.org/10.1016/0257-8972(95)02646-0

[3] Evans, H. E., and Taylor, M. P., "Diffusion Cells and Chemical Failure of MCrAlY Bond Coats in Thermal-Barrier Coating Systems," *Oxidation of Metals*, Vol. 55, Nos. 1–2, 2001, pp. 17–34. https://doi.org/10.1023/A:1010369024142

[4] Padture, N. P., Gell, M., and Jordan, E. H., "Thermal Barrier Coatings for Gas-Turbine Engine Applications," *Science*, Vol. 296, No. 5566, 2002, pp. 280–284. https://doi.org/10.1126/science.1068609

[5] Ma, W., and Dong, H., "2–Ceramic Thermal Barrier Coating Materials," *Thermal Barrier Coatings*, edited by H. Xu, and H. Guo, Woodhead Publishing, Oxford, 2011, pp. 25–52.

[6] Naraparaju, R., Hüttermann, M., Schulz, U., and Mechnich, P., "Tailoring the EB-PVD Columnar Microstructure to Mitigate the Infiltration of CMAS in 7YSZ Thermal Barrier Coatings," *Journal of the European Ceramic Society*, Vol. 37, No. 1, 2017, pp. 261–270. https://doi.org/10.1016/j.jeurceramsoc.2016.07.027

[7] Wang, L., Guo, L., Li, Z., Peng, H., Ma, Y., Gong, S., and Guo, H., "Protectiveness of Pt and Gd2Zr2O7 Layers on EB-PVD YSZ Thermal Barrier Coatings Against Calcium–Magnesium–Alumina–Silicate (CMAS) Attack," *Ceramics International*, Vol. 41, No. 9, 2015, pp. 11662–11669. https://doi.org/10.1016/j.ceramint.2015.05.128

[8] Zhang, D., "1–Thermal Barrier Coatings Prepared by Electron Beam Physical Vapor Deposition (EB–PVD)," *Thermal Barrier Coatings*, edited by H. Xu, and H. Guo, Woodhead Publishing, Oxford, 2011, pp. 3–24.

[9] Zhang, G., Fan, X., Xu, R., Su, L., and Wang, T. J., "Transient Thermal Stress Due to the Penetration of Calcium-Magnesium-Alumino-Silicate in EB-PVD Thermal Barrier Coating System," *Ceramics International*, Vol. 44, No. 11, 2018, pp. 12655–12663. https://doi.org/10.1016/j.ceramint.2018.04.065

[10] Zhao, H., Levi, C. G., and Wadley, H. N., "Molten Silicate Interactions with Thermal Barrier Coatings," *Surface and Coatings Technology*, Vol. 251, July 2014, pp. 74–86. https://doi.org/10.1016/j.surfcoat.2014.04.007

[11] Bose, S., *High Temperature Coatings*, Butterworth-Heinemann, Oxford, 2017.

[12] Liu, Q., Huang, S., and He, A., "Composite Ceramics Thermal Barrier Coatings of Yttria Stabilized Zirconia for Aero-Engines," *Journal of Materials Science & Technology*, Vol. 35, No. 12, 2019, pp. 2814–2823. https://doi.org/10.1016/j.jmst.2019.08.003

[13] Gong, S., and Wu, Q., "6–Processing, Microstructures and Properties of Thermal Barrier Coatings by Electron Beam Physical Vapor Deposition (EB–PVD)," *Thermal Barrier Coatings*, edited by H. Xu, and H. Guo, Woodhead Publishing, Oxford, 2011, pp. 115–131.

[14] Mercer, C., Faulhaber, S., Evans, A., and Darolia, R., "A Delamination Mechanism for Thermal Barrier Coatings Subject to Calcium–Magnesium–Alumino-Silicate (CMAS) Infiltration," *Acta Materialia*, Vol. 53, No. 4, 2005, pp. 1029–1039. https://doi.org/10.1016/j.actamat.2004.11.028

[15] Krämer, S., Faulhaber, S., Chambers, M., Clarke, D. R., Levi, C. G., Hutchinson, J. W., and Evans, A. G., "Mechanisms of Cracking and Delamination Within Thick Thermal Barrier Systems in Aero-engines Subject to Calcium-maGNESIUM-ALUmino-Silicate (CMAS) Penetration," *Materials Science and Engineering: A*, Vol. 490, Nos. 1–2, 2008, pp. 26–35. https://doi.org/10.1016/j.msea.2008.01.006

[16] Borom, M. P., Johnson, C. A., and Peluso, L. A., "Role of Environment Deposits and Operating Surface Temperature in Spallation of Air Plasma Sprayed Thermal Barrier Coatings," *Surface and Coatings Technology*, Vol. 86, Dec. 1996, pp. 116–126. https://doi.org/10.1016/S0257-8972(96)02994-5

[17] Mohan, P., Yuan, B., Patterson, T., Desai, V. H., and Sohn, Y. H., "Degradation of Yttria–Stabilized Zirconia Thermal Barrier Coatings by Vanadium Pentoxide, Phosphorous Pentoxide, and Sodium Sulfate," *Journal of the American Ceramic Society*, Vol. 90, No. 11, 2007, pp. 3601–3607. https://doi.org/10.1111/j.1551-2916.2007.01941.x

[18] Krämer, S., Yang, J., Levi, C. G., and Johnson, C. A., "Thermochemical Interaction of Thermal Barrier Coatings with Molten CaO–MgO–Al2O3–SiO2 (CMAS) Deposits," *Journal of the American Ceramic

Society, Vol. 89, No. 10, 2006, pp. 3167–3175.
https://doi.org/10.1111/j.1551-2916.2006.01209.x

[19] Shinozaki, M., Roberts, K. A., van de Goor, B., and Clyne, T. W., "Deposition of Ingested Volcanic Ash on Surfaces in the Turbine of a Small Jet Engine," *Advanced Engineering Materials*, Vol. 15, No. 10, 2013, pp. 986–994.
https://doi.org/10.1002/adem.201200357

[20] Bansal, N. P., and Choi, S. R., "Properties of CMAS Glass from Desert Sand," *Ceramics International*, Vol. 41, No. 3, 2015, pp. 3901–3909.
https://doi.org/10.1016/j.ceramint.2014.11.072

[21] Wiesner, V. L., and Bansal, N. P., "Mechanical and Thermal Properties of Calcium–Magnesium Aluminosilicate (CMAS) Glass," *Journal of the European Ceramic Society*, Vol. 35, No. 10, 2015, pp. 2907–2914.
https://doi.org/10.1016/j.jeurceramsoc.2015.03.032

[22] Naraparaju, R., Gomez Chavez, J. J., Schulz, U., and Ramana, C. V., "Interaction and Infiltration Behavior of Eyjafjallajökull, Sakurajima Volcanic Ashes and a Synthetic CMAS Containing FeO with/in EB-PVD ZrO2-65 wt% Y2 O3 Coating at High Temperature," *Acta Materialia*, Vol. 136, Sept. 2017, pp. 164–180.
https://doi.org/10.1016/j.actamat.2017.06.055

[23] Yin, B., Liu, Z., Yang, L., Wu, R., and Zhou, Y., "Factors Influencing the Penetration Depth of Molten Volcanic Ash in Thermal Barrier Coatings: Theoretical Calculation and Experimental Testing," *Results in Physics*, Vol. 13, June 2019, Paper 102169.
https://doi.org/10.1016/j.rinp.2019.102169

[24] Wellman, R., Whitman, G., and Nicholls, J. R., "CMAS Corrosion of EB PVD TBCs: Identifying the Minimum Level to Initiate Damage," *International Journal of Refractory Metals and Hard Materials*, Vol. 28, No. 1, 2010, pp. 124–132.
https://doi.org/10.1016/j.ijrmhm.2009.07.005

[25] Qu, W., Li, S., Chen, Z., Li, C., Pei, Y., and Gong, S., "Hot Corrosion Behavior and Wettability of Calcium–Magnesium–Alumina–Silicate (CMAS) on LaTi2Al9O19 Ceramic," *Corrosion Science*, Vol. 162, Jan. 2020, Paper 108199.
https://doi.org/10.1016/j.corsci.2019.108199

[26] Xu, G. N., Yang, L., Zhou, Y. C., Pi, Z. P., and Zhu, W., "A Chemo-Thermo-Mechanically Constitutive Theory for Thermal Barrier Coatings Under CMAS Infiltration and Corrosion," *Journal of the Mechanics and Physics of Solids*, Vol. 133, Dec. 2019, Paper 103710.
https://doi.org/10.1016/j.jmps.2019.103710

[27] Yin, B., Zhang, F., Zhu, W., Yang, L., and Zhou, Y., "Effect of Al2O3 Modification on the Properties of YSZ: Corrosion Resistant, Wetting and Thermal-Mechanical Properties," *Surface and Coatings Technology*, Vol. 357, Jan. 2019, pp. 161–171.
https://doi.org/10.1016/j.surfcoat.2018.09.048

[28] Zhang, X. F., Zhou, K. S., Liu, M., Deng, C. M., Deng, C. G., and Deng, Z. Q., "Adsorbability and Spreadability of Calcium-Magnesium-Alumino-Silicate (CMAS) on Al-Modified 7YSZ Thermal Barrier Coating," *Ceramics International*, Vol. 42, No. 16, 2016, pp. 19349–19356.
https://doi.org/10.1016/j.ceramint.2016.09.106

[29] Naraparaju, R., Schulz, U., Mechnich, P., Döbber, P., and Seidel, F., "Degradation Study of 7 wt.% Yttria Stabilised Zirconia (7YSZ) Thermal Barrier Coatings on Aero-Engine Combustion Chamber Parts Due to Infiltration by Different CaO–MgO–Al2O3–SiO2 Variants," *Surface and Coatings Technology*, Vol. 260, Dec. 2014, pp. 73–81.
https://doi.org/10.1016/j.surfcoat.2014.08.079

[30] Naraparaju, R., Mechnich, P., Schulz, U., and Mondragon Rodriguez, G. C., "The Accelerating Effect of CaSO4 Within CMAS (CaO–MgO–Al2O3–SiO2) and Its Effect on the Infiltration Behavior in EB–PVD 7YSZ," *Journal of the American Ceramic Society*, Vol. 99, No. 4, 2016, pp. 1398–1403.
https://doi.org/10.1111/jace.14077

[31] Naraparaju, R., Pubbysetty, R. P., Mechnich, P., and Schulz, U., "EB-PVD Alumina (Al2O3) as a Top Coat on 7YSZ TBCs Against CMAS/VA Infiltration: Deposition and Reaction Mechanisms," *Journal of the European Ceramic Society*, Vol. 38, No. 9, 2018, pp. 3333–3346.
https://doi.org/10.1016/j.jeurceramsoc.2018.03.027

[32] Naraparaju, R., Gomez Chavez, J. J., Niemeyer, P., Hess, K. U., Song, W., Dingwell, D. B., Lokachari, S., Ramana, C. V., and Schulz, U., "Estimation of CMAS Infiltration Depth in EB-PVD TBCs: A New Constraint Model Supported with Experimental Approach," *Journal of the European Ceramic Society*, Vol. 39, No. 9, 2019, pp. 2936–2945.
https://doi.org/10.1016/j.jeurceramsoc.2019.02.040

[33] Jackson, R. W., Zaleski, E. M., Poerschke, D. L., Hazel, B. T., Begley, M. R., and Levi, C. G., "Interaction of Molten Silicates with Thermal Barrier Coatings Under Temperature Gradients," *Acta Materialia*, Vol. 89, May 2015, pp. 396–407.
https://doi.org/10.1016/j.actamat.2015.01.038

[34] Jackson, R. W., Zaleski, E. M., Hazel, B. T., Begley, M. R., and Levi, C. G., "Response of Molten Silicate Infiltrated Gd2Zr2O7 Thermal Barrier Coatings to Temperature Gradients," *Acta Materialia*, Vol. 132, June 2017, pp. 538–549.
https://doi.org/10.1016/j.actamat.2017.03.081

[35] Giordano, D., Russell, J. K., and Dingwell, D. B., "Viscosity of Magmatic Liquids: A Model," *Earth and Planetary Science Letters*, Vol. 271, Nos. 1–4, 2008, pp. 123–134.
https://doi.org/10.1016/j.epsl.2008.03.038

[36] Zhu, Z., "Study of Volcanic Ash Impact onto Turbine Blades in Jet Engines," Ph.D. Dissertation, Dept. of Chemical and Process Engineering, Univ. of Surrey, Guildford, U.K., 2019.

[37] Cheng, Y., Wang, F., Xu, J., Liu, D., and Sui, Y., "Numerical Investigation of Droplet Spreading and Heat Transfer on Hot Substrates," *International Journal of Heat and Mass Transfer*, Vol. 121, June 2018, pp. 402–411.
https://doi.org/10.1016/j.ijheatmasstransfer.2018.01.026

[38] Choi, M., Son, G., and Shim, W., "A Level-Set Method for Droplet Impact and Penetration into a Porous Medium," *Computers & Fluids*, Vol. 145, March 2017, pp. 153–166.
https://doi.org/10.1016/j.compfluid.2016.12.014

[39] Herreros, M. I., Mabssout, M., and Pastor, M., "Application of Level-Set Approach to Moving Interfaces and Free Surface Problems in Flow Through Porous Media," *Computer Methods in Applied Mechanics and Engineering*, Vol. 195, No. 1, 2006, pp. 1–25.
https://doi.org/10.1016/j.cma.2004.12.015

[40] Wiesner, V. L., Vempati, U. K., and Bansal, N. P., "High Temperature Viscosity of Calcium-Magnesium-Aluminosilicate Glass from Synthetic Sand," *Scripta Materialia*, Vol. 124, Nov. 2016, pp. 189–192.
https://doi.org/10.1016/j.scriptamat.2016.07.020

[41] Masoodi, R., and Pillai, K. M., "Traditional Theories of Wicking: Capillary Models," *Wicking in Porous Materials: Traditional and Modern Modeling Approaches*, CRC Press, Taylor & Francis Group, Boca Raton, FL, 2012, pp. 31–53.

[42] Zhang, B., Song, W., and Guo, H., "Wetting, Infiltration and Interaction Behavior of CMAS Towards Columnar YSZ Coatings Deposited by Plasma Spray Physical Vapor," *Journal of the European Ceramic Society*, Vol. 38, No. 10, 2018, pp. 3564–3572.
https://doi.org/10.1016/j.jeurceramsoc.2018.04.01

[43] Dvorkin, J., "*Kozeny-Carman Equation Revisited*," Stanford Univ., Stanford, CA, 2009 (unpublished).

[44] Rayleigh, L., "LVI. On the Influence of Obstacles Arranged in Rectangular Order Upon the Properties of a Medium," *London, Edinburgh, and Dublin Philosophical Magazine and Journal of Science*, Vol. 34, No. 211, 1892, pp. 481–502.
https://doi.org/10.1080/14786449208620364

[45] Renteria, A. F., Saruhan, B., Schulz, U., Raetzer-Scheibe, H.-J., Haug, J., and Wiedenmann, A., "Effect of Morphology on Thermal Conductivity of EB-PVD PYSZ TBCs," *Surface and Coatings Technology*, Vol. 201, No. 6, 2006, pp. 2611–2620.
https://doi.org/10.1016/j.surfcoat.2006.05.003

[46] Kolagar, A. M., Tabrizi, N., Cheraghzadeh, M., and Shahriari, M. S., "Failure Analysis of Gas Turbine First Stage Blade Made of Nickel-Based Superalloy," *Case Studies in Engineering Failure Analysis*, Vol. 8, April 2017, pp. 61–68.
https://doi.org/10.1016/j.csefa.2017.04.002

[47] Gupta, S., Chaube, A., and Verma, P., "Review on Heat Transfer Augmentation Techniques: Application in Gas Turbine Blade Internal Cooling," *Journal of Engineering Science & Technology Review*, Vol. 5, No. 1, 2012, pp. 57–62.

[48] Forsbacka, L., Holappa, L., Iida, T., Kita, Y., and Toda, Y., "Experimental Study of Viscosities of Selected CaO–MgO–Al2O3–SiO2 SLAGS and application of the IIDA Model," *Scandinavian Journal of Metallurgy*, Vol. 32, No. 5, 2003, pp. 273–280.
https://doi.org/10.1034/j.1600-0692.2003.00652.x

[49] Guo, L., Yan, Z., Yu, Y., Yang, J., and Li, M., "CMAS Resistance Characteristics of LaPO4/YSZ Thermal Barrier Coatings at 1250°C–1350°C," *Corrosion Science*, Vol. 154, July 2019, pp. 111–122.
https://doi.org/10.1016/j.corsci.2019.04.014.

[50] Kakuda, T. R., Levi, C. G., and Bennett, T. D., "The Thermal Behavior of CMAS-Infiltrated Thermal Barrier Coatings," *Surface and Coatings Technology*, Vol. 272, June 2015, pp. 350–356.
https://doi.org/10.1016/j.surfcoat.2015.03.043

[51] Kucuk, A., Clare, A., and Jones, L., "An Estimation of the Surface Tension for Silicate Glass Melts at 1400°C Using Statistical Analysis," *Glass Technology*, Vol. 40, No. 5, 1999, pp. 149–153.

[52] Bogard, D. G., and Thole, K. A., "Gas Turbine Film Cooling," *Journal of Propulsion and Power*, Vol. 22, No. 2, 2006, pp. 249–270.
https://doi.org/10.2514/1.18034

[53] Peng, H., Wang, L., Guo, L., Miao, W., Guo, H., and Gong, S., "Degradation of EB-PVD Thermal Barrier Coatings Caused by CMAS Deposits," *Progress in Natural Science: Materials International*, Vol. 22, No. 5, 2012, pp. 461–467.
https://doi.org/10.1016/j.pnsc.2012.06.007

[54] Schulz, U., Fritscher, K., Leyens, C., and Peters, M., "Influence of Processing on Microstructure and Performance of Electron Beam Physical Vapor Deposition (EB-PVD) Thermal Barrier Coatings," *Journal of Engineering for Gas Turbines and Power*, Vol. 124, No. 2, 2002, pp. 229–234.
https://doi.org/10.1115/1.1447238

[55] Gildersleeve, E., Viswanathan, V., and Sampath, S., "Molten Silicate Interactions with Plasma Sprayed Thermal Barrier Coatings: Role of Materials and Microstructure," *Journal of the European Ceramic Society*, Vol. 39, No. 6, 2019, pp. 2122–2131.
https://doi.org/10.1016/j.jeurceramsoc.2019.01.023

Queries

1. AU: Please note that an acronym is not allowed in the main title and was spelled out.

2. AU: Please check that the copyright (©) type is correct. Please note that the code will be added upon publication.

3. AU: Because AIAA requires abstracts to be written in the third person, the last sentence has been edited to reflect this. Please confirm the change retains your meaning, or else review and edit further to clarify.

4. AU: Please differentiate the superscripts from the subscripts. “Superscripts” will be the final heading. Please move the appropriate entries beneath it. “Subscripts” should be the heading before “Superscripts”, per AIAA requirements.

5. AU: Because AIAA does not permit more than one “=” sign in a single entry in the Nomenclature, entries have been amended to reflect this. Please confirm the changes retain your meaning, or else review and edit further to clarify.

6. AU: References [50, 51] was not cited in the main text. Please cite the reference in the main text (which does not include the Conclusions section, figures, or tables) in numerical order or remove the reference.

7. AU: Please note that AIAA requires acronyms be used more than once to remain in the paper.

8. AU: Because AIAA requires a colon be used only if the clause can stand alone as a complete sentence, clauses preceding display equations have been edited throughout. Please confirm the changes retain your meaning, or else review and edit further to clarify.

9. AU: Eqs. 1 and 2 citations have been changed to Eqs. A1 and A2, to conform to Appendix standard labels for equations. Please confirm this change is correct, or review and edit if necessary, if the main Eqs. 1 and 2 were meant.

10. AU: Please review and edit “The time needed to penetration top 200 μm” for clarity.

11. AU: Table A1 is not cited in this paper. Please cite the table in the Appendix text or main text (which does not include the Conclusions section, figures, or tables) or remove it.

12. AU: For Ref. [11, 43], please provide the page range and/or chapter number.

Funding Information

The following research funding sources have been associated with your manuscript:

- National Science Foundation; Award no. CBET-1705538; Funder ID http://dx.doi.org/10.13039/100000001

Funding sources listed here can be 1) research grants from outside agencies or organizations or 2) if an author is employed by a U.S. government agency that directly funded this research, this employer also may be listed here as a funding agency. Please confirm that this information is complete and correct for all authors. Edit the Funding Data/Acknowledgments section of your paper if you have changes to funding agency names or grant numbers. Use the funder’s full and official name.